Accepted Manuscript

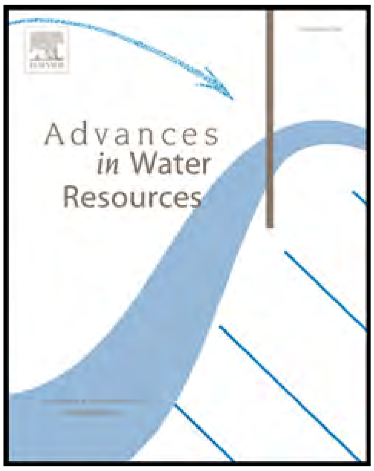

Porous gravity currents: axisymmetric propagation in horizontally graded medium and a review of similarity solutions

I. Lauriola, G. Felisa, D. Petrolo, V. Di Federico, S. Longo

PII: S0309-1708(17)30871-0
DOI: 10.1016/j.advwatres.2018.03.008
Reference: ADWR 3111

To appear in: *Advances in Water Resources*

Received date: 8 September 2017
Revised date: 3 March 2018
Accepted date: 4 March 2018

Please cite this article as: I. Lauriola, G. Felisa, D. Petrolo, V. Di Federico, S. Longo, Porous gravity currents: axisymmetric propagation in horizontally graded medium and a review of similarity solutions, *Advances in Water Resources* (2018), doi: 10.1016/j.advwatres.2018.03.008

Highlights

- Axisymmetric gravity currents of power-law fluid in domain with horizontal permeability variation
- Self-similar solutions are derived as functions of model parameters
- Theoretical results for radius and profile are validated by experiments
- A review on porous gravity currents of power-law fluid is carried out
- Key parameters governing the dynamics of power-law gravity currents are compared

Porous gravity currents: axisymmetric propagation in horizontally graded medium and a review of similarity solutions

I. Lauriola[a], G. Felisa[a], D. Petrolo[b], V. Di Federico[a], S. Longo[b]

[a]*Dipartimento di Ingegneria Civile, Chimica, Ambientale e dei Materiali (DICAM), Università di Bologna, Viale Risorgimento, 2, 40136 Bologna, Italy*
[b]*Dipartimento di Ingegneria e Architettura (DIA), Università di Parma, Parco Area delle Scienze, 181/A, 43124 Parma, Italy*

Abstract

We present an investigation on the combined effect of fluid rheology and permeability variations on the propagation of porous gravity currents in axisymmetric geometry. The fluid is taken to be of power-law type with behaviour index n and the permeability to depend from the distance from the source as a power-law function of exponent β. The model represents the injection of a current of non-Newtonian fluid along a vertical bore hole in porous media with space-dependent properties. The injection is either instantaneous ($\alpha = 0$) or continuous ($\alpha > 0$). A self-similar solution describing the rate of propagation and the profile of the current is derived under the assumption of small aspect ratio between the current average thickness and length. The limitations on model parameters imposed by the model assumptions are discussed in depth, considering currents of increasing/decreasing velocity, thickness, and aspect ratio, and the sensitivity of the radius, thickness, and aspect ratio to model parameters. Several critical values of α and β discriminating between opposite tendencies are thus determined. Experimental validation is performed using shear-thinning suspensions and Newtonian mixtures in different regimes. A box filled with ballotini of different diameter is used to reproduce the current, with observations from the side and bottom. Most experimental results for the radius and profile of the current agree well with the self-similar solution except at the beginning of the process, due to the limitations of the 2-D assumption and to boundary effects near the injection zone. The results for this specific case corroborate a general model for currents with constant or time-varying volume of power-law fluids propagating in porous domains of plane or radial geometry, with uniform or varying permeability, and the possible effect of channelization. All results obtained in the present and previous papers for the key parameters governing the dynamics of power-law gravity currents are summarized and compared to infer the combinations of parameters leading to the fastest/lowest rate of propagation, and of variation of thickness and aspect ratio.

Keywords: gravity current, self similar, non-Newtonian, experiment, review

1. Introduction

The propagation of gravity-driven flows in porous media is but a chapter of the fascinating 'book' on gravity currents (hereinafter GCs), which has received considerable attention [1], with new 'chapters' being continuously added. Yet also porous GCs by themselves, originating from such diverse applications (carbon dioxide sequestration, mining engineering, environmental pollution and remediation, seawater intrusion, to name but a few) constitute such a wide topic that a comprehensive summary is arduous. In the authors' view, the recent advancements on gravity-driven porous flow belong to two broad categories.

The first group of contributions has as a common feature the modelling of the spatial variations of properties and/or of boundary conditions in natural (geologic) media, and the description of their topographical features. Examples of such contributions are Huppert *et al.* [2], Sahu and Flynn [3], and Ngo *et al.* [4], where heterogeneity is modelled via discrete layers or intrusions of finite extent; Islam *et al.* [5], who introduce explicitly small-scale heterogeneity; Yu *et al.* [6], who account simultaneously for drainage from a permeable substrate and an edge; and Huber *et al.* [7], who aim at reproducing the effect of diverse CO_2 injection strategies.

The second broad group of GC-themed contributions presents an improved description of fundamental mechanisms via a more sophisticated modelling. Some relevant examples are the effects of a change in flux (Ball *et al.* [8]) or of stratification in an intruding current (Pegler *et al.* [9]); the investigation of the CO_2 sequestration mechanisms into deep saline aquifers, involving two-phase flow (Guo *et al.* [10]) or with possible background hydrological flow (Unwin *et al.* [11]); the interactions between gravity currents and convective dissolution (Elenius *et al.*, [12]), or geomechanics (Bjornara *et al.* [13]); the adoption of realistic rheological models in the study of non-Newtonian GCs (Di Federico *et al.* [14]).

Some recent contributions belong to both categories, and are associated, for example, with the modelling of CO_2 sequestration [4] or the simultaneous presence of non-Newtonian flow and spatial heterogeneity or specific topographical features. The latter topic has been investigated in depth in several papers, considering deterministic heterogeneity and radial [15] or plane geometry [16], and channelized flow [15]. The motivation for these studies lies in a multiplicity of applications involving complex fluids flowing in geologic media characterized by spatial heterogeneity at various scales: oil and displacing suspensions in reservoir flow, remediation carriers and liquid contaminants in the subsurface environments, drilling and grouting fluids; earlier works [15, 16] list specific references to these applications.

Studies of flows of non-Newtonian GCs rely on a body of knowledge accumulated for Newtonian currents: the reference works of Huppert & Woods [17] for plane geometry, and by Lyle *et al.* [18] for axisymmetric geometry, were extended to power-law fluid flow by Di Federico *et al.* [19, 20], which, in turn, set the stage for the more complex setups cited earlier. Variations of properties along vertical and horizontal direction were considered in the context of Newtonian GCs by Zheng *et al.* [21, 22]. While vertical variations mimic the effect of stratification, horizontal variations may represent e.g. the effect induced by the drilling of a well, and thus are of interest especially in the context of axisymmetric propagation. A review of existing studies on non-Newtonian porous GCs reveals the lack of a study coupling power-law rheology and permeability gradients along the flow direction in axisymmetric flow. Such a study is presented here in Sections 2-5 considering the usual hypothesis of a GC of time-variable inflow.

The exposition is organized as follows. The mathematical problem is formulated in section 2 for a radial injection, and solved in section 3 in self-similar form generalizing the results of Di Federico *et al.* [20]. Section 4 discusses the dependency of key time exponents governing the propagation of the current on problem parameters, along with the limitations imposed by modelling assumptions. Experimental results are presented in Section 5; first, the experimental set-up is described, with special attention on the difficulties implied by simulating heterogeneity; then results from a series of tests are compared with the theory in constant- and variable-flux regime.

The theory and experiments presented complete a first picture on porous gravity currents of power-law fluid flowing in different geometries (plane and axisymmetric) in domains exhibiting permeability variations in different directions (vertical and horizontal), taking into account the influence of the channel cross section for plane flow. A general overview and comparison of these self-similar solutions seems timely, and is presented in Section 6. Concluding remarks are formulated in Section 7 together with perspectives for future work.

2. Problem formulation

Consider a non-Newtonian power-law fluid of density ρ, consistency index m, and flow behavior index n, that spreads axisymmetrically over a horizontal bed into a porous medium of height h_0, initially saturated with a lighter fluid of density $\rho - \Delta\rho$ (see Figure 1). Under the sharp interface and thin current approximations, and in the absence of capillary effects (see the recent paper by Chiapponi [23] for an indication of the fluid retention in a glass beads porous medium), the pressure within the current is hydrostatic, and given by $p(r, z, t) = p_1 + \Delta\rho\, gh(r, t) - \rho gz$, where r and z represent radial and vertical coordinates, $p_1 = p_0 + (\rho - \Delta\rho)gh_0$ is a constant, p_0 is the constant pressure at $z = h_0$, and g is gravity. Under the additional assumption that the current thickness is small compared to that of the ambient fluid, the velocity of the latter and the vertical velocity in the intruding fluid can be neglected, allowing to describe the current behaviour by means of its horizontal velocity $u(r, t)$, thickness $h(r, t)$ and maximum extension $r_N(t)$ for given time t. The expression of the horizontal velocity can be deduced from the following general equation, valid for the motion of a power-law fluid in a porous medium [24]

$$\nabla p - \rho \boldsymbol{g} = -\frac{\mu_{eff}}{k}|\boldsymbol{u}|^{n-1}\boldsymbol{u}, \tag{1}$$

in which p is the pressure, $\boldsymbol{u}$ is the Darcy velocity field, $\boldsymbol{g}$ is the gravity vector, k the permeability, and μ_{eff} is the effective viscosity (dimensions $[\mathrm{ML}^{-n}\mathrm{T}^{n-2}]$). The mobility $\frac{\mu_{eff}}{k}$ is given by [20]

$$\frac{k}{\mu_{eff}} = \frac{1}{2C_t}\frac{1}{m}\left(\frac{n\phi}{3n+1}\right)^n \left(\frac{50k}{3\phi}\right)^{(n+1)/2}, \tag{2}$$

where ϕ is the porosity and $C_t = C_t(n)$ the tortuosity factor. The modified Darcy's law (1) is based on a capillary bundle model first proposed by Bird *et al.* [25] and later modified to include tortuosity, for which different formulations are available (e.g. Shenoy, 1995 [26]); in the following, the formulation by Pascal, 1983 [27], $C_t = (25/12)^{(n+1)/2}$, is adopted. Macroscopic laws having the same structure of Eq.(1) were obtained via direct simulation at the pore scale by e.g. Balhoff and Thompson [28] and Vakilha and Manzari [29]. Experimental verification was provided, among others, by Cristopher and Middleman [24] and Yilmaz *et al.* [30]. Additional references on the use of Eq. (1) are reported in [20]. The model is unable to handle viscoelastic effects and thixotropy, and needs to be modified to include yield stress or Newtonian behaviour at low shear rates.

Local mass conservation implies that

$$\frac{1}{r}\frac{\partial}{\partial r}\left(ruh\right) = -\phi\frac{\partial h}{\partial t}, \tag{3}$$

and, in addition, two boundary conditions are needed to formulate the problem. The first b.c. is the global mass conservation condition

$$2\pi\phi\int_0^{r_N(t)} rh(r,t)\mathrm{d}r = Qt^{\alpha}, \tag{4}$$

expressing the total volume of the current as a function of time t and parameters Q (dimensions $[\mathrm{L}^3\mathrm{T}^{-\alpha}]$) and α. This formulation includes the instantaneous injection with constant volume ($\alpha = 0$), and the continuous injection with increasing volume ($\alpha > 0$).

The second boundary condition states that the thickness at the current front is null, i.e.

$$h\left(r_N(t), t\right) = 0. \tag{5}$$

Further, the horizontal permeability variation needs to be described. The following law of variation is adopted for the medium permeability k [31, 22]

$$k(r) = k_0\left(\frac{r}{\sigma r^*}\right)^{\beta}, \tag{6}$$

where k_0 is a characteristic permeability, r^* is a length scale, σ is a coefficient introduced for convenience, and β is a constant. The coefficient σ is necessary in order to recover the dependency of the permeability only on the characteristics of the porous medium, and assumes different values for different length scales r^* in order to keep the denominator σr^* independent on the fluid properties and on the injection power-law. For $\beta \lesseqgtr 0$, the permeability decreases or increases with the distance from the injection well, respectively;

$\beta = 0$ represents a medium with constant permeability k_0, and the simpler model of Di Federico *et al.* [20] is recovered. For $\beta < 0$, the behaviour of (6) is singular for $r \to 0$, but this does not affect the overall behaviour of the current. Further, we require that $\beta < \beta_0 = 2(n+3)/(n+1)$; this upper limitation to the increase of the permeability with distance from the origin guarantees the validity of our solution from a theoretical point of view, as demonstrated in Section 4.1. For a Newtonian fluid ($n = 1$), $\beta_0 = 4$ (Ciriello *et al.* [31] found $\beta_0 = 3$ in plane geometry); for the two limit cases $n \ll 1$ and $n \gg 1$ (very shear-thinning or shear-thickening fluids), $\beta_0 \sim 6$ and $\beta_0 \sim 2$ respectively. In a related study on Newtonian gravity currents in Hele-Shaw cells with a gap thickness varying in the flow direction, Zheng *et al.* [22] showed that the upper limit for the validity of the lubrication approximation is $\beta < 3$ in terms of the present paper. They then derived results for β=0.6, 1.5, and 2.4, a range of values including the actual β value simulated in our experiments described in Section 5.

As far as field values are concerned, realistic exponents for vertical power-law variations of properties [32, 33] tend to be much lower than the upper limit value β_0. More importantly, also horizontal variations of permeability are often modelled with negative exponential or decreasing power-law functions, to represent the steadily decreasing permeability, altered by the drilling process, of the aquifer around a large diameter well [34, 35] or of the reservoir surrounding a fracture [36]). In both cases, there is a simplification of the actual behaviour, where probably a constant and lower value of permeability is reached at a certain distance from the well or fracture.

Substituting Eq.(6) in the one-dimensional version of Eq.(1), and expressing the pressure gradient as a function of the unknown free surface as $\partial p/\partial r = \Delta\rho\, g(\partial h/\partial r)$ yields the following equation of motion

$$u(r, z, t) = -\left(\mathit{\Lambda}\Delta\rho\, g\right)^{1/n} k_0^{(n+1)/(2n)} \left(\frac{r}{\sigma r^*}\right)^{\frac{\beta(n+1)}{2n}} \left|\frac{\partial h}{\partial r}\right|^{1/n-1} \frac{\partial h}{\partial r}, \qquad (7)$$

where

$$\mathit{\Lambda} = \mathit{\Lambda}(\phi, m, n) = \frac{1}{2C_t}\left(\frac{50}{3}\right)^{(n+1)/2}\left(\frac{n}{3n+1}\right)^n \frac{\phi^{(n-1)/2}}{m}, \qquad (8)$$

which for a Newtonian fluid ($n = 1$) is the inverse of dynamic viscosity μ .

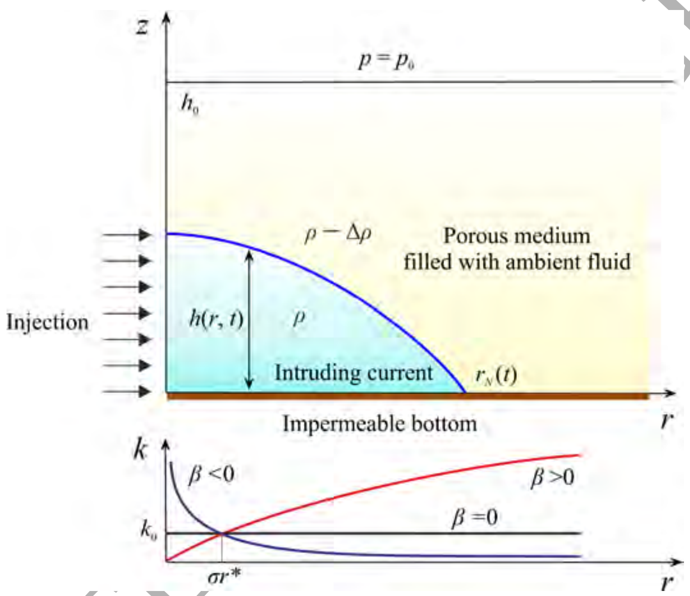

Figure 1: Sketch of an axisymmetric gravity current intruding into a saturated porous medium of thickness h_0. The bottom panel illustrates radially increasing ($\beta > 0$), decreasing ($\beta < 0$), and homogeneous ($\beta = 0$) permeabilities.

The mathematical problem constituted by Equations (7) and (3) with boundary conditions (4) and (5) may be rendered non-dimensional upon defining time, space, and velocity scales as

$$t^* = \left(\frac{Q}{\phi v^{*3}}\right)^{1/(3-\alpha)}, \; r^* = v^* t^*, \; v^* = \frac{(\mathit{\Lambda}\Delta\rho\, g)^{1/n} k_0^{(1+n)/(2n)}}{\phi \sigma^{\beta(n+1)/(2n)}}, \tag{9}$$

and dimensionless coordinates as $T = t/t^*$, $R = r/r^*$, $R_N = r_N/r^*$, and $H = h/r^*$.

Note that the time scale t^* is defined for $\alpha \neq 3$. The particular case $\alpha = 3$ requires a partially different non-dimensional formulation, which can be easily derived following, e.g. [19, 37]. For all other cases, the dimensionless problem reads

$$\frac{1}{R}\frac{\partial}{\partial R}\left[R^{F_1+1} H \left|\frac{\partial H}{\partial R}\right|^{1/n-1} \frac{\partial H}{\partial R}\right] = \frac{\partial H}{\partial T}, \tag{10}$$

obtained by combining the dimensionless versions of (7) and (3). In Eq. (10)

$$F_1 = \frac{\beta(n+1)}{2n} \tag{11}$$

is a factor which reduces to zero in the homogeneous case.

The global mass balance (4) becomes

$$2\pi \int_0^{R_N} RH \mathrm{d}R = T^\alpha, \tag{12}$$

while the condition at the front (5) becomes $H(R_N) = 0$ in dimensionless form.

3. Solution

It is desirable to obtain a self-similar solution to the system formed by Equations (10) and (12) with (5) to capture the long-term evolution of the current once the influence of initial and boundary conditions fades. As illustrated in the Appendix, a first-kind similarity solution for the extension and thickness of the current is derived in the form $R_N(T) = \eta_N T^{F_2}$ and $H(R,T) = \eta_N^{F_5} T^{F_3} \psi(\zeta)$, where the thickness factor $\psi(\zeta)$ is the solution of the non linear ordinary differential equation

$$\left(\zeta^{F_1+1}\psi\psi' \left|\psi'\right|^{1/n-1}\right)' + F_2\zeta^2\psi' - F_3\zeta\psi = 0, \tag{13}$$

in which the prime indicates d $/\mathrm{d}\zeta$, and subject to the condition

$$\psi(1) = 0, \tag{14}$$

while the similarity variable at the front of the current η_N is given by

$$\eta_N = \left(2\pi \int_0^1 \zeta\psi(\zeta)\mathrm{d}\zeta\right)^{-1/(F_5+2)}, \tag{15}$$

and the factors F_2, F_3 and F_5 are given by (A.2), (A.3), and (A.7), respectively. For a homogeneous medium ($\beta = 0$), results reduce to the simpler case of Di Federico *et al.* [20], with $F_1 = 0$, $F_2 = (\alpha+n)/(n+3)$, $F_3 = [\alpha(n+1) - 2n]/(n+3)$, and $F_5 = n+1$. For a Newtonian fluid ($n = 1$), one obtains $F_1 = \beta$, $F_2 = (\alpha+1)/(4-\beta)$, $F_3 = [\alpha(2-\beta)-2]/(4-\beta)$, and $F_5 = 2-\beta$. When both simplifications apply, the homogeneous Newtonian case studied by Lyle *et al.* [18] is recovered, and $F_1 = 0$, $F_2 = (\alpha+1)/4$, $F_3 = (\alpha-1)/2$, and $F_5 = 2$.

For the instantaneous injection case ($\alpha = 0$), Equations (13) and (15) subject to (14) and $\psi'(0) = 0$ (the latter condition derives from a no-flux boundary condition for $r = 0$, valid for constant volume) are amenable to the closed-form solution

$$\psi(\zeta) = \frac{F_{20}^n}{F_5}\left(1-\zeta^{F_5}\right), \tag{16}$$

$$\eta_N = \left(\frac{\pi F_{20}^n}{F_5+2}\right)^{-\frac{1}{F_5+2}}, \tag{17}$$

where $F_{20} = F_2(\alpha = 0) = 2n/[2(n+3) - \beta(n+1)]$. The constraint $F_5 > 0$ (equivalent to $\beta < 2$) applies. When $\beta = 0$, Eq. (17) of Di Federico *et al.* [20] is recovered. When $n = 1$, (16) and (17) transform into

$$\psi(\zeta) = \frac{1}{(4-\beta)(2-\beta)}\left(1-\zeta^{2-\beta}\right), \tag{18}$$

$$\eta_N = \left[\frac{(4-\beta)^2}{\pi}\right]^{1/(4-\beta)}. \tag{19}$$

Finally when both $n = 1$ and $\beta = 0$, $\psi(\zeta) = (1-\zeta^2)/8$ and $\eta_N = 2/\pi^{1/4}$ [38].

For the continuous injection case ($\alpha \neq 0$) equation (13) needs to be integrated numerically with (14) and a second boundary condition is obtained expanding the solution in power Frobenius series and balancing the lower order terms for $\zeta \to 1$. This yields

$$\psi'|_{\zeta\to 1} = -a_0 b \epsilon^{b-1},\ a_0 = F_2^n,\ b = 1, \tag{20}$$

where $\epsilon = 1-\zeta$ is a small quantity and F_2 is non-negative if $\beta < 2(n+3)/(n+1)$. Integrating (13) with (14) and (20) with a Runge-Kutta scheme yields the thickness profile $\psi(\zeta)$ and the similarity variable η_N. Sample results are shown in Figures 2(a)-(f) for $\alpha = 0, 1$, and selected values of n and β. The analytical solution for $\alpha = 0$ and the results obtained by Lyle *et al.* [18] for the Newtonian, homogeneous case are well reproduced. The thickness profile $\psi(\zeta)$ increases with the injected volume (α) for given fluid and medium (n and β), is an increasing function of β, and a decreasing function of n for constant volume currents; the dependency on n for constant flux currents is more complex. The prefactor η_N (15), whose value influences the current thickness via (A.8), is illustrated in Figure 2(g) versus α for different n, β. η_N increases with n and decreases with α and β, while its sensitivity is largest for smaller α and n and larger β. These dependencies are reversed with respect to the thickness profile, so that the dimensionless thickness results from the interplay of ψ and η_N.

Other quantities of interest are the aspect ratio of the current (the ratio between its average thickness $\overline{H}$ and radius R_N) and the average free-surface gradient driving the motion $\overline{\left(\frac{\partial H}{\partial R}\right)}$. These are given respectively by

$$\frac{\overline{H}}{R_N} = \eta_N^{F_5-1} T^{F_3-F_2} \overline{\psi}, \tag{21}$$

$$\overline{\left(\frac{\partial H}{\partial R}\right)} = \eta_N^{F_5-1} T^{F_3-F_2} \overline{\left(\frac{d\psi}{d\zeta}\right)};\ F_3 - F_2 = \frac{\alpha[2n-\beta(n+1)]-6n}{2(n+3)-\beta(n+1)}, \tag{22}$$

where $\overline{\psi}$ and $\overline{\left(\frac{d\psi}{d\zeta}\right)}$ are respectively the average value of the thickness profile and of its derivative over the interval 0-1.

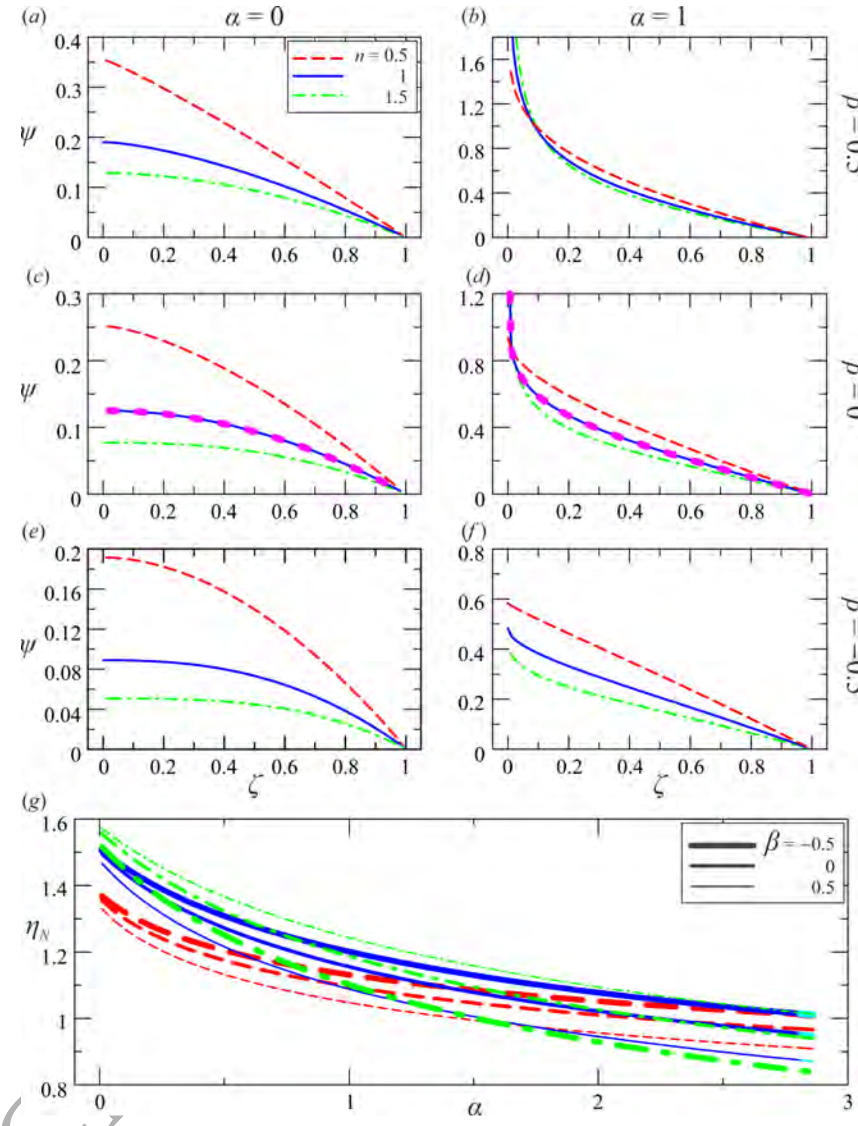

Figure 2: (a)-(f) Thickness profile $\psi(\zeta)$. Upper/intermediate/lower rows: radially increasing ($\beta = 0.5$)/uniform ($\beta = 0$)/decreasing ($\beta = -0.5$) permeability; left/right columns: constant volume ($\alpha = 0$)/constant flux ($\alpha = 1$); dashed red/solid light blue/dot-dashed green lines: shear-thinning ($n = 0.5$)/Newtonian ($n = 1$)/shear-thickening ($n = 1.5$) fluids. Pink ovals in panels (c)-(d) are the results by Lyle *et al.* [18] for $\beta = 0, n = 1$ and $\alpha = 0, 1$, respectively;(g) prefactor $\eta_N(\alpha)$. Dashed/solid/dash-dotted lines: $n = 0.5/1/1.5$; thick/intermediate/thin lines: $\beta = 0.5/0/0.5$. (Colour online)

Furthermore, the velocity field u is given in dimensionless form $U = u/v^*$ by

$$U = -\phi R^{F_1} \eta_N^{\frac{F_5-1}{n}} T^{\frac{F_3-F_2}{n}} \left|\frac{\partial\psi}{\partial\zeta}\right|^{1/n-1} \frac{\partial\psi}{\partial\zeta}, \tag{23}$$

while for the velocity of advancement of the front of the current, $v = \mathrm{d}\, r_N(t)/\mathrm{d}\, t$, the dimensionless expression $V = v/v^*$ is

$$V = \eta_N F_2 T^{F_2-1}, \text{ with } F_2 - 1 = \frac{2\alpha - [6-\beta(n+1)]}{(n+1)(2-\beta)+4}. \tag{24}$$

4. Discussion of results

4.1. Behaviour of key time exponents

The power-law time exponents F_2, $F_2 - 1$, F_3 and $F_3 - F_2$ (equations (A.2), (24), (A.3), and (22)), of the radius, velocity, thickness and aspect ratio of the gravity current are the key factors to understand the evolution of the current over time. In the present section, we explore their dependency on model parameters α (the time rate of change of the fluid volume), n (the flow behaviour index), and β (the rate of change of the permeability along the direction of propagation) by evaluating their sign and their partial derivatives with respect to model parameters. The results obtained for F_2 (together with $F_2 - 1$), F_3, and $F_3 - F_2$ are listed in Tables 1, 2, and 3, respectively. Various limit values of α, and, in some instances, of other parameters, emerge; each limit value is listed below the respective condition on F_2, F_3, $F_3 - F_2$ or their partial derivative. These threshold values of model parameters discriminate between a positive, null, or negative value of F_2, F_3, $F_3 - F_2$ and of their partial derivative with respect to α, n, and β.

Inspection of Table 1 reveals that for a physically meaningful solution, the permeability must decrease over space, or increase not too sharply ($\beta < \beta_e$); for a Newtonian fluid ($n = 1$), $\beta_e = 4$. The current front accelerates ($F_2 - 1 > 0$) for any α under a sharp increase in permeability ($\beta > \beta_a$), or beyond a threshold value α_a of α for permeability decreasing or increasing moderately over space ($\beta < \beta_a$); otherwise, the current is decelerated. For a Newtonian fluid ($n = 1$), the threshold values reduce to $\beta_a = 3$, $\alpha_a = 3 - \beta$; for a homogeneous medium ($\beta = 0$) and any fluid, $\alpha_a = 3$. Moreover, F_2 increases with α for any combination of β, n, as a larger fluid injection rate implies an increase in the current velocity regardless of the permeability variation and fluid nature. Similarly, F_2 increases with β for any combination of

Table 1: Dependence of the propagation rate F_2 on model parameters for horizontally varying permeability. For each row, limits on model parameters necessary to achieve the condition itemized in column 1 are listed in column 2; when appropriate, the value(s) of specific threshold parameters is/are also listed in the same row. Row 1: Conditions for $F_2 > 0$. Row 2: conditions for decelerated/constant speed/accelerated currents. Row 3: condition for F_2 increasing with α. Row 4: conditions for F_2 decreasing/constant/increasing with n. Row 5: conditions for F_2 increasing with β.

(1)	$F_2 > 0$	$\beta < \beta_e$
	β_e	$\dfrac{n+3}{n+1}$
(2)	$F_2 - 1 < 0$	$\beta < \beta_a \wedge \alpha < \alpha_a$
	$F_2 - 1 = 0$	$\beta < \beta_a \wedge \alpha = \alpha_a$
	$F_2 - 1 > 0$	$(\beta < \beta_a \wedge \alpha > \alpha_a) \vee (\beta = \beta_a \wedge \alpha > 0) \vee$ $(\beta > \beta_a \wedge \forall \alpha)$
	β_a	$\dfrac{6}{n+1}$
	$\alpha_a(\beta < \beta_a)$	$\dfrac{6 - \beta(n+1)}{2}$
(3)	$\dfrac{\partial F_2}{\partial \alpha} > 0$	$\forall n, \beta$
(4)	$\dfrac{\partial F_2}{\partial n} < 0$	$\beta < \beta_{en} \wedge \alpha > \alpha_{en}$
	$\dfrac{\partial F_2}{\partial n} = 0$	$\beta < \beta_{en} \wedge \alpha = \alpha_{en}$
	$\dfrac{\partial F_2}{\partial n} > 0$	$(\beta < \beta_{en} \wedge \alpha < \alpha_{en}) \vee (\beta \geq \beta_{en} \wedge \forall \alpha)$
	β_{en}	2
	$\alpha_{en}(\beta < \beta_{en})$	$\dfrac{6 - \beta}{2 - \beta}$
(5)	$\dfrac{\partial F_2}{\partial \beta} > 0$	$\forall \alpha, n$

Table 2: Dependence of the thickness time exponent F_3 on model parameters for horizontally varying permeability. For each row, limits on model parameters necessary to achieve the condition itemized in column 1 are listed in column 2; when appropriate, the value(s) of specific threshold parameters is/are also listed in the same row. Row 1: conditions for thickness decreasing/constant/increasing with time. Row 2: condition for F_3 decreasing/constant/increasing with α. Row 3: conditions for F_3 decreasing/constant/increasing with n. Row 4: conditions for F_3 decreasing with β.

(1)	$F_3 < 0$	$(\beta < \beta_t \wedge \alpha < \alpha_t) \vee (\beta \geq \beta_t \wedge \forall\alpha)$
	$F_3 = 0$	$\beta < \beta_t \wedge \alpha = \alpha_t$
	$F_3 > 0$	$\beta < \beta_t \wedge \alpha > \alpha_t$
	β_t	2
	$\alpha_t(\beta < \beta_t)$	$\dfrac{4n}{(n+1)(2-\beta)}$
(2)	$\dfrac{\partial F_3}{\partial \alpha} \lesseqgtr 0$	$\beta \gtreqless \beta_t$
	$\beta_{t\alpha}$	2
(3)	$\dfrac{\partial F_3}{\partial n} < 0$	$(\beta < \beta_{tn} \wedge \alpha < \alpha_{tn}) \vee (\beta \geq \beta_{tn} \wedge \forall\alpha)$
	$\dfrac{\partial F_3}{\partial n} = 0$	$\beta < \beta_{tn} \wedge \alpha = \alpha_{tn}$
	$\dfrac{\partial F_3}{\partial n} > 0$	$\beta < \beta_{tn} \wedge \alpha > \alpha_{tn}$
	β_{tn}	2
	$\alpha_{tn}(\beta < \beta_{tn})$	$\dfrac{6-\beta}{2-\beta}$
(4)	$\dfrac{\partial F_3}{\partial \beta} < 0$	$\forall\alpha, n$

Table 3: Dependence of the aspect ratio time exponent $F_3 - F_2$ on model parameters for horizontally varying permeability. For each row, limits on model parameters necessary to achieve the condition itemized in column 1 are listed in column 2; when appropriate, the value(s) of specific threshold parameters is/are also listed in the same row. Row 1: conditions for aspect ratio increasing/constant/decreasing with time. Row 2: condition for $F_3 - F_2$ increasing with α. Row 3: conditions for $F_3 - F_2$ decreasing/constant/increasing with n. Row 4: conditions for $F_3 - F_2$ decreasing/constant/increasing with β.

$$
(1)\begin{cases}
F_3 - F_2 < 0 & (\beta < \beta_g \wedge \alpha < \alpha_g) \vee (\beta \geq \beta_g \wedge \forall\alpha) \\
F_3 - F_2 = 0 & \beta < \beta_g \wedge \alpha = \alpha_g \\
F_3 - F_2 > 0 & \beta < \beta_g \wedge \alpha > \alpha_g \\
\beta_g & \dfrac{2n}{n+1} \\
\alpha_g(\beta < \beta_g) & \dfrac{6n}{2n - \beta(n+1)}
\end{cases}
$$

$$
(2)\begin{cases}
\dfrac{\partial(F_3 - F_2)}{\partial\alpha} \lesseqqgtr 0 & \beta \gtreqqless \beta_{g\alpha} \\
\beta_{g\alpha} & \dfrac{2n}{n+1}
\end{cases}
$$

$$
(3)\begin{cases}
\dfrac{\partial(F_3 - F_2)}{\partial n} < 0 & (\beta < \beta_{gn} \wedge \alpha < \alpha_{gn}) \vee (\beta \geq \beta_{gn} \wedge \forall\alpha) \\
\dfrac{\partial(F_3 - F_2)}{\partial n} = 0 & \beta < \beta_{gn} \wedge \alpha = \alpha_{gn} \\
\dfrac{\partial(F_3 - F_2)}{\partial n} > 0 & \beta < \beta_{gn} \wedge \alpha > \alpha_{gn} \\
\beta_{gn} & 2 \\
\alpha_{gn}(\beta < \beta_{gn}) & \dfrac{6-\beta}{2-\beta}
\end{cases}
$$

$$
(4)\begin{cases}
\dfrac{\partial(F_3 - F_2)}{\partial\beta} < 0 & \forall\alpha, n
\end{cases}
$$

α, n, as an increase/less marked decrease of the permeability favours the current advancement. The functional dependency of F_2 on n is more complex, as the velocity of the current increases with n for any α under a sharp increase in permeability ($\beta > \beta_{en}$), or below a threshold value α_{en} of α for permeability decreasing or increasing moderately over space ($\beta < \beta_{en}$). The current velocity decreases with n when combining a large injection rate ($\alpha > \alpha_{en}$) with a permeability decreasing or increasing moderately over space ($\beta < \beta_{en}$). For a Newtonian fluid ($n = 1$), the threshold value of α reduces to $\alpha_{en} = 3$.

Inspection of Table 2 shows that the thickness of the current increases with time at a given point ($F_3 > 0$) only when a large injection rate ($\alpha > \alpha_t$) is combined with permeability decreasing or increasing moderately over space ($\beta < \beta_t$); for decreasing permeability, the current encounters more resistance as it advances, while for a moderately increasing permeability, the decrease in medium resistance is more than compensated by the volume increase of the current. In all other cases, the thickness decreases over time, and does so for any α when the permeability increase is marked. For a Newtonian fluid ($n = 1$), the threshold value of α reduces to $\alpha_t = 2/(2-\beta)$; for a homogeneous medium ($\beta = 0$) and any fluid, $\alpha_t = 2n/(n + 1)$. Furthermore, it is noted that F_3 decreases or increases with α depending whether a threshold value α_t is exceeded or not, or, equivalently, depending whether the increase in the volume of the current prevails over the permeability increase along the flow direction. The functional dependency of F_3 on n is the opposite of F_2 and the same threshold values due to mass balance. Finally, F_3 decreases with β for any combination of α, n, as an increase/less marked decrease of the permeability increases the radius of the current, thus implying a decrease in thickness due to mass balance. For the same reasons, the dependence of F_3 upon n is the opposite of F_2, with the threshold value α_{tn} being equal to α_{en}.

Inspection of Table 3 indicates that the aspect ratio/average spatial gradient of the current increases with time ($F_3 - F_2 > 0$) only when a large injection rate ($\alpha > \alpha_g$) is combined with permeability decreasing or increasing moderately over space ($\beta < \beta_g$); this behaviour can be understood noting that the average spatial gradient is proportional to the resistance encountered by the current in its advancement. Otherwise, the aspect ratio decreases with time, and the current grows progressively more elongated. For a Newtonian fluid ($n = 1$), the threshold values reduce to $\alpha_g = 2/(2 - \beta)$, $\beta_g = 1$; for a homogeneous medium ($\beta = 0$) and any fluid, $\alpha_g = 3$. The dependence of $F_3 - F_2$ on α is governed by a threshold value $\beta_{g\alpha}$; for $\beta > \beta_{g\alpha}$, $F_3 - F_2$ decreases with increasing α; the reverse is true for $\beta < \beta_{g\alpha}$. This is so because unless the permeability increase is marked, the aspect ratio of the current increases with the injection rate. The threshold is $\beta > \beta_{g\alpha} = 1$ for a Newtonian fluid. The behaviour of $F_3 - F_2$ as a function of n is analogous to F_2, with the same threshold values. Finally, $F_3 - F_2$ decreases with β for any combination of α, n, as a more permeable medium implies less resistance to the flow and a reduced average spatial gradient.

To visually illustrate the behaviour of the key exponent, Figures 3(a)-(f) depict how F_2, F_3 and $F_3 - F_2$ depend on β for fixed $n = 0.5$ and on n for fixed $\beta = -0.5$; results for various values of α, including the critical ones, are shown. The two reference values ($n = 0.5$ and $\beta = -0.5$) are selected for illustrative purposes and represent common cases in natural porous media, i.e. a shear-thinning fluid and a permeability decreasing with distance from the source.

A comparison of the threshold values of α and β reveals that: i) for a homogeneous medium ($\beta = 0$), all threshold values of α coalesce into 3, except for α_t; ii) for a Newtonian fluid ($n = 1$), the threshold values of α are β-dependent; iii) for Newtonian flow in a homogeneous medium, $\alpha_t = 1$. A plot of the limit α_g is shown in Figure 4 for $n = 0.5$, 1, 1.5. The limiting value of α increases with β; the increase is more rapid for $\beta > 0$. The influence of n on α_g is mixed, in that this limit value increases with n for $\beta < 0$ and decreases with n for $\beta > 0$. For a homogeneous medium, the limit α_g is independent of the behaviour index n.

4.2. Limits of validity

Limitations on the parameters emerge when considering the validity of model assumptions. At any time, conditions for the radius of the current to increase with time must hold ($F_2 > 0$), as noted in the previous subsection. Furthermore, for $T \gg 1$ the thin current approximation requires the intruding current to be thin compared to both its height ($F_3 - F_2 < 0$) and the characteristic height h_0 of the porous medium ($F_3 < 0$). Otherwise, at large times i) the current thickness would exceed a reasonable portion of the porous domain total height, rendering invalid the assumption of immobile ambient fluid; ii) the aspect ratio of the current would increase without bounds, contrary to the assumption of negligible vertical velocities. Combining these limitations, the parameters domain satisfying all model assumptions asymptotically (the most restrictive condition) is obtained. An example is illustrated in Figure 5, where the two limits β_e and β_g are depicted, the first

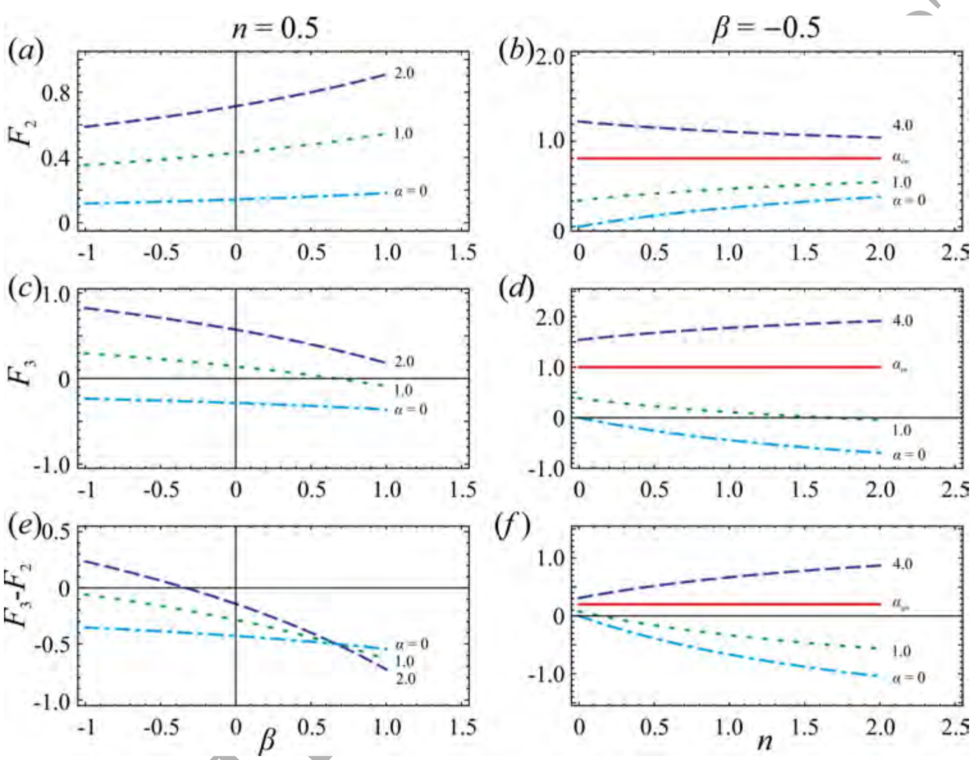

Figure 3: (a)-(f) The value of the time exponents F_2, F_3 and $F_3 - F_2$ for a current with length $\propto T^{F_2}$, height $\propto T^{F_3}$, mean free-surface gradient/aspect ratio $\propto T^{F_3 - F2}$, and volume $\propto T^{\alpha}$ in a porous medium with permeability varying horizontally as r^{β}. Results are shown for F_2, F_3 and $F_3 - F_2$ in the upper, intermediate and lower rows, respectively, as a function of β for $n = 0.5$ and as a function of n for $\beta = -0.5$ (left and right columns, respectively), and for different values of α. $\alpha_{en} = \alpha_{tn} = \alpha_{gn} = (6 - \beta)/(2 - \beta)$

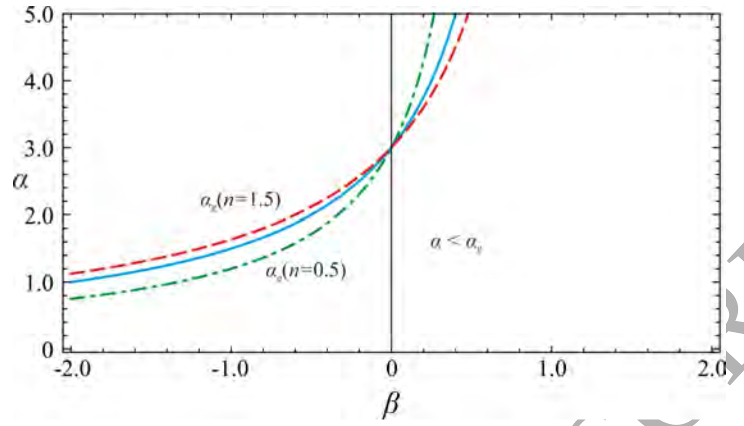

Figure 4: Limiting values of α to ensure an asymptotic decrease of the average steepness of the current, $\alpha < \alpha_g$ and $\beta < \beta_g$.

to ensure $F_2 > 0$, the second to ensure $F_3 - F_2 < 0$; in all cases of practical interest ($n < 3$) the latter limitation is more stringent than the former. It is seen that a too sharp increase in the permeability along the flow direction renders the current steeper with time; the limit β value is 0.67 for $n = 0.5$ and 1 for $n = 1$.

4.3. Limitations of the model for in-situ applications

As to in-situ applications, there is still room to improve the connection between the present model and the field conditions. The model is based on a monotonic permeability variation from the well to infinity (porosity variations can be easily added), and is not presently able to handle composite and more complex spatial variations. When the permeability variation is due to fracturing/rearrangement of grains during drilling or due to sealing, or to mud injection in the medium, a cutoff is expected at a certain distance from the well. In addition, in the latter cases the most relevant variations of permeability and porosity happen at a short distance from the well, where the model itself is questionable due to several effects earlier highlighted. However, in other cases the permeability reduction is more gradual, for example when it is associated to clogging of pore space resulting from deposition of fine material or escape of dissolved gases in water aquifers. Nevertheless the results are promising and indicate that further steps and advancements can be based on the present approach, which can function as a benchmark solution for more complex situations; more on this in the Conclusions.

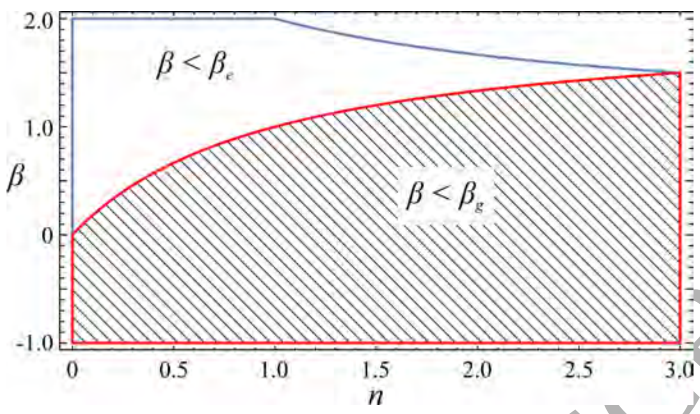

Figure 5: Limiting values of β to ensure a positive time advancing of the front of the current, $\beta < \beta_e \equiv (n+3)/(n+1)$, and an asymptotic decreasing average steepness of the current, $\beta < \beta_g \equiv 2n/(n+1)$.

5. Laboratory experiments

5.1. Experimental setup

A series of experiments were conducted at the Hydraulic Laboratory of the University of Parma, to test the validity of the theoretical solution.

A 90° sector glass tank 25 cm × 25 cm × 25 cm in size was filled with transparent glass ballotini with nominal diameters of $d = 1.0, 2.0, 3.0, 4.0$ and 5.0 mm to reproduce a porous medium. The continuous horizontal gradient of the permeability required by Eq. (6) was approximately reproduced by using a plastic framework that allowed to create separate neighbouring sectors, each filled with beads of uniform diameter and having uniform permeability given by the Kozeny-Carman equation. The thickness of each sector was determined according to the procedure outlined in Appendix B of [15], which provides the connection between the geometry of the stepwise distribution of diameters and the the theoretical parameters k_0 and β of the continuous distribution (6).

The plastic framework shown in Figure 6 consists of thin plastic sheets (0.5 mm) curved in order to reproduce four quarters of cylinder with radius equal to 3.2 cm, 6 cm, 9 cm and 12.2 cm, with two radial diaphragms (plane plastic sheets). After filling the sectors with the beads, the framework is gently removed by lifting it. Figure 7 shows the radial distribution of the diameters and the permeability for $\beta = 1.65$. The diameters adopted for the

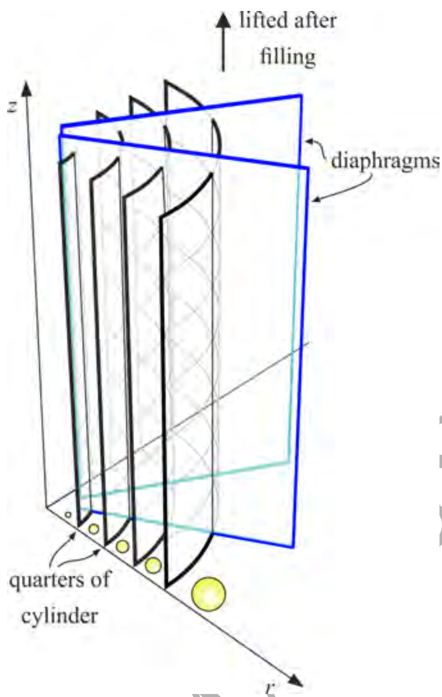

Figure 6: Plastic frame used to fill the tank with ballotini of different diameter in the radial direction and with axisymmetric configuration.

beads are in the upper range for natural porous media; this choice mainly reflects commercial availability and ease of sieving. Nevertheless the solution is applicable to porous media with grains of any size as long as the underlying assumptions are respected. The horizontality of the bottom of the tank was checked by an electronic level. The intruding current was a shear-thinning fluid, made of softened water (water without cations like Ca^{++} and Mg^{++}), glycerine and Xanthan Gum, mixed in two different proportions: (i) 40% (vol) of water, 60% (vol) of glycerine and 0.10% (weight) of Xanthan Gum, (ii) 95% (vol) of water, 5% (vol) of glycerine and 0.15% (weight) of Xanthan Gum. Ink was added to the final mixture for an easy visualization and detection of the interface. We used a commercial Xanthan Gum for food use from a local supplier, and glycerine was added to increase the consistency index without adding too much Xanthan Gum. The mixing was performed in a low speed stirrer, by adding small quantities of Xanthan Gum to pure water and then adding glycerine. After mixing, lumps were removed with a

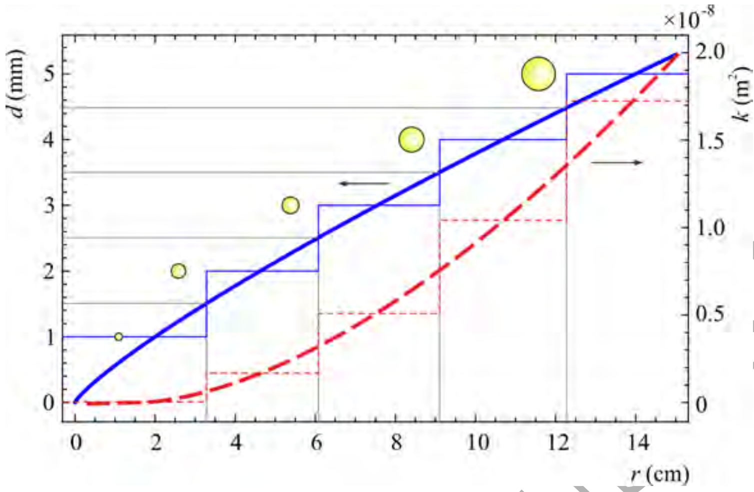

Figure 7: Radial distribution of the diameter of the ballotini (continuous thick curve) and of the permeability (dashed thick curve) for $\beta = 1.65$ and $k_0 = 1.986 \times 10^{-8}\,\mathrm{m}^2$. The curves are the interpolation of the step functions representing diameter and permeability (thin curves), since the diameter of the ballotini is constant within each vertical sector.

small colander and the mixture was left at rest for several hours. The overall result is that mixtures with the same ingredients, but prepared in different days, show different rheological parameters. The rheological parameters (flow behaviour index n and consistency index m) were measured by a strain-controlled rheometer (Dynamic Shear Rheometer, Anton Paar Physica MCR 101), with parallel plates roughened by sandpaper P-60 glued onto both smooth surfaces. The distance between the plates was 1 mm and the testing temperature of the rheometer was $T = 25°\mathrm{C}$, equal to the one measured in the laboratory during the experiments, with expected fluctuations of $\pm 1°\mathrm{C}$. The range of shear rate during measurements was chosen in order to overlap the range of shear rate expected during flow in the porous medium, following the criterion reported in [39]. According to this criterion, the effective shear rate should be evaluated at the pore scale, by using, e.g., the expression given by Savins (1969) [40]

$$\dot{\gamma} = \frac{u\sqrt{2 \times 10^{-4}}}{\sqrt{k\phi c'}}, \tag{25}$$

with u the Darcian velocity and $c' = 2.1 - 2.4$ a coefficient related to tortu-

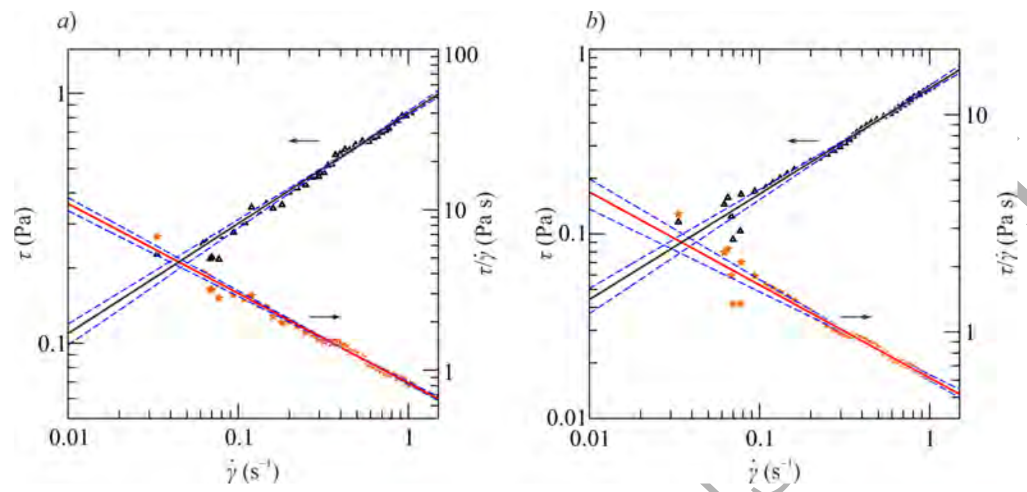

Figure 8: Stress-strain (triangles) and apparent viscosity (stars) measurements *a*) for the fluid used in Exp. A4, and *b*) for the fluid used in Exp. B2–B4. The dashed lines are the 95% confidence limits of the interpolating power–law functions $\tau = 0.82\,\dot{\gamma}^{0.43}$ and $\tau = 0.62\,\dot{\gamma}^{0.57}$, respectively. One point in three is shown for an easy visualization.

osity. The result is a low effective shear rate in most part of the body of the current (see Longo *et al.*, 2013 [39], Figure 5, for an estimation of the shear rate in experiments similar to the present experiments). Indeed in some part of the current, like the injection area, the shear rate is much larger than in the body of the current. However, it has been experimentally demonstrated that the evolution of a viscous-buoyancy gravity current is not influenced by the local disturbances near the inlet section, see, e.g., Lyle *et al.*, 2005 [18]. Figure 8 shows the stress-strain measurements for two fluids adopted in the experiments, with the interpolating power–law function. We bear in mind that the power–law approximation hides a much more complex rheological behaviour of the mixture, see, e.g., [41, 42], which is also influenced by ions and chemicals. Hence, the power–law is adopted as a pragmatic working tool for a simple and synthetic description of the local rheology of the fluid.

The intruding fluid was injected with a syringe pump into the tank through a quarter-cylinder volume similar to a well having radius of 0.8 cm, obtained with a brass net, which was located in one corner of the tank. This configuration reproduces an axisymmetric spreading due to the symmetry along the the vertical axis and with negligible influence of the wall boundary layers.

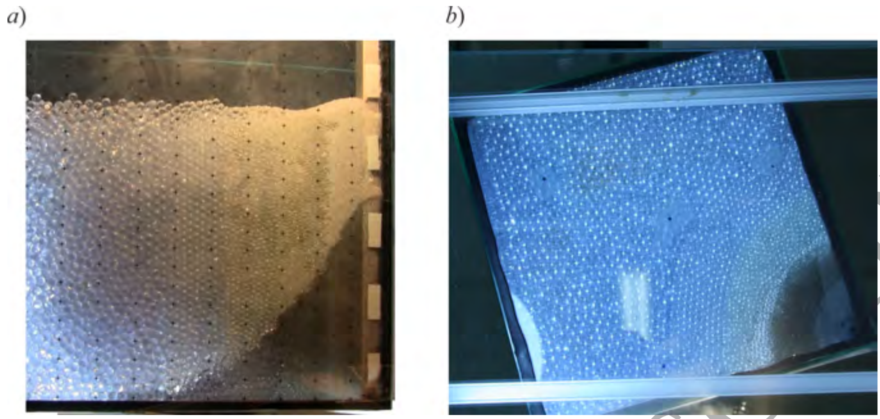

Figure 9: Typical images of the side- (a) and bottom-view (b) for one of the experiments. The radial increment of the diameter of the ballotini can be observed in both images.

The syringe pump was controlled by an analog electric signal to generate a constant ($\alpha = 1$) or waxing ($\alpha = 1.5, 2.0$) influx rate. During the injection, the lateral current profile was recorded by a high-resolution video-camera (Canon Legria HF 20, 1920×1080 pixels) working at 25 frames per second, while the bottom view was reflected by a mirror and captured by a photo-camera shooting every 2 seconds. The videos and images were post-processed using a software to transform the pixel positions into metric coordinates. A grid stuck on the wall and on the bottom of the tank was used to reconstruct the correspondence between image and physical plane surfaces, with the use of interpolating polynomials functions. The position of the front of the current was detected by selecting the nose on the image and then converting the pixels coordinates into metric coordinates, with an overall accuracy of ± 1 mm.

Figure 9 shows two typical images of the side- and bottom-view during one of the experiments.

5.2. Experimental results and discussion

A total of 10 experiments were performed, with the experimental parameters summarized in Table 4. The horizontal permeability is controlled by the value of β, which was kept constant for all data sets, while the injection rate (α), the fluid rheology (m and n), and the fluid density (ρ) varied among the tests. Figure 10 depicts the non dimensional front position R_N of the current for the various tests, compared with the theoretical prediction. For most tests, with the exception of A1 and A4, experimental results indicate a front position below the theoretical counterpart before reaching it asymptotically in all cases. The good agreement between theoretical and experimental data over time (asymptotically within 5%) is due to the balance of buoyancy and viscous forces, while the disturbing effects due to injection, with significant vertical velocity, influence the position of the front only at the beginning of motion. The comparison between tests A4 and B3, which only differ in the type of fluid (having respectively $n \approx 0.43$ and $n \approx 0.57$), leads to the conclusion that the more shear-thinning fluid (A4) best fits the theoretical model, and this result holds true since the beginning of the test. Furthermore, shear-thinning fluids advance slower with decreasing values of n, as shown upon comparing tests A5 and B4 for $\alpha \geq 2$.

The results of tests A2 and A3, characterized by different values of Q, i.e. 2.4 and 4.0 $\mathrm{cm}^3\,\mathrm{s}^{-1}$, clearly show the same behaviour, demonstrating that, all other parameters being equal, Q is not relevant in the evaluation of the dimensionless front position R_N. Indeed, a little variation of density, e.g. between tests B2 and B5, proves that the fluid density ρ significantly affects the dimensionless position of the front. The comparison between the actual position of the front end among different experiments is best performed in dimensional form, as the time and velocity scales are function of experimental parameters, which differ among the tests conducted.

Figure 11*ab* shows the shape of the current at different times for two experiments with constant and waxing influx rate, respectively. The agreement between experiments and model is fairly good, in particular at late times. Near the origin the experimental shape of the current is below the theoretical profile, even though this effect does not affect significantly the front end position and the shape of the main body.

6. Overview on non-Newtonian gravity currents in porous media

The present section is devoted to an overview of self-similar solutions governing the propagation of non-Newtonian currents of variable volume with power-law rheology in porous media. The overview is performed by comparing the key parameters governing the propagation, i.e. F_2, F_3 and $F_3 - F_2$, equal to the time exponents of the extension, thickness, and slope of the current (derivation of the exponent of the velocity of the front end of the current, $F_2 - 1$, is trivial) for a variety of combinations of geometries and

Exp.	Q $(\mathrm{cm}^3\,\mathrm{s}^{-\alpha})$	α	m $(\mathrm{Pa\ s}^n)$	n	ρ $(\mathrm{g\ cm}^{-3})$	β
A1	1.20	1.01	0.071 ± 0.004	1.00 ± 0.01	1.221 ± 0.001	1.65
A2	2.40	1.02	0.80 ± 0.02	0.45 ± 0.02	1.176	1.65
A3	4.00	1.00	0.78 ± 0.02	0.48 ± 0.02	1.176	1.65
A4	0.64	1.53	0.82 ± 0.02	0.43 ± 0.02	1.176	1.65
A5	0.029	2.05	1.02 ± 0.02	0.23 ± 0.01	1.176	1.65
B1	2.40	1.01	1.21 ± 0.02	0.80 ± 0.03	1.086	1.65
B2	3.08	1.01	0.62 ± 0.01	0.57 ± 0.02	1.086	1.65
B3	0.64	1.53	0.62	0.57	1.086	1.65
B4	0.030	2.03	0.62	0.57	1.086	1.65
B5	4.01	1.00	0.64 ± 0.01	0.56 ± 0.02	1.088	1.65

Table 4: Experimental parameters. Q is a coefficient of the time varying volume Qt^α, α is the time exponent ($\alpha = 1$ means constant influx rate), m and n are the consistency and the fluid behaviour index, respectively, ρ is the mass density of the fluid and β is a parameter controlling the radial variation of the permeability. The uncertainty listed for some of the values refers to one standard deviation.

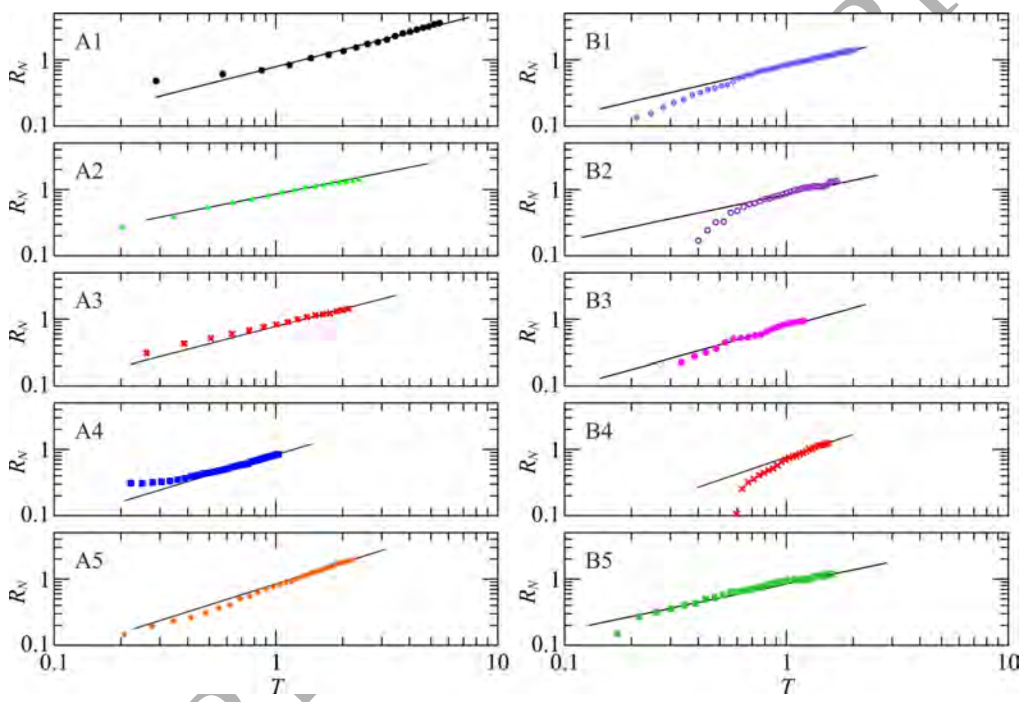

Figure 10: The non dimensional front position of the current. The symbols represent the experiments, the solid lines the theoretical data. The parameters of the experiments are listed in Table 4.

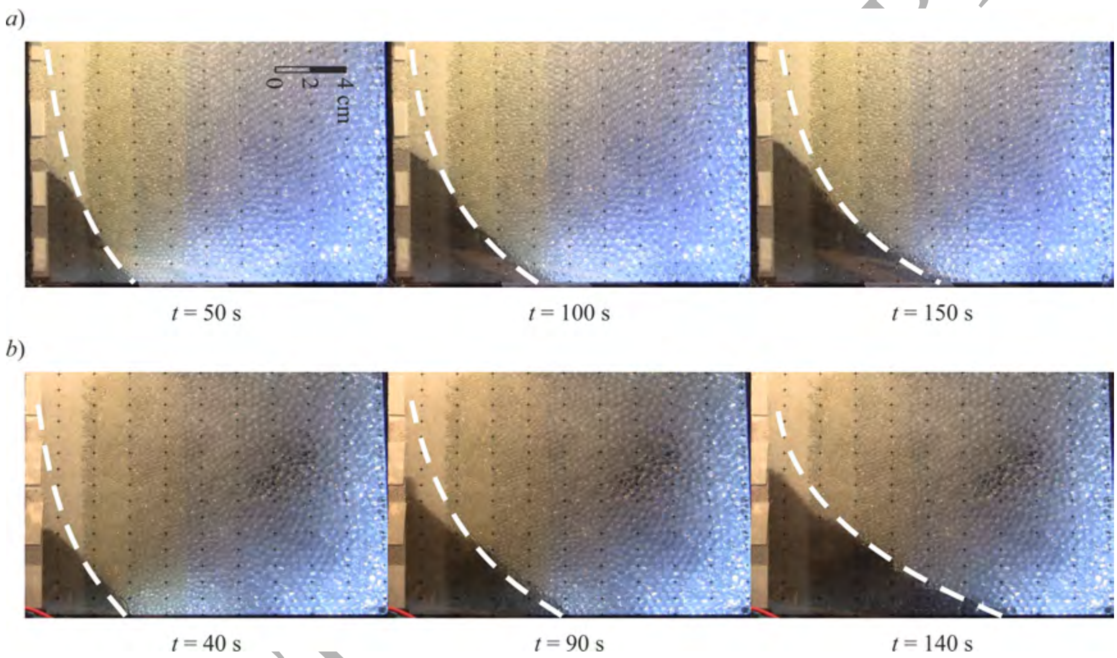

Figure 11: Theoretical (dashed line) versus experimental current shape for *a*) Exp. A2, constant influx rate ($\alpha = 1$), and *b*) Exp. A5, waxing influx rate ($\alpha = 2.05$).

	Plane unbounded [19]	*Plane channelized* [43]	*Plane, vertical heterogeneity* [16]	*Plane, horizontal heterogeneity* [16]
F_2	$\frac{\alpha+n}{n+2}$	$\frac{\alpha\kappa+n(\kappa+1)}{n+1+\kappa(n+2)}$	$\frac{\alpha[(n+1)(\omega-1)+2]+2n}{2(n+2)+(n+1)(\omega-1)}$	$\frac{2(\alpha+n)}{2(n+2)-\beta(n+1)}$
F_3	$\frac{\alpha(n+1)-n}{n+2}$	$\frac{\kappa[\alpha(n+1)-n]}{n+1+\kappa(n+2)}$	$\frac{2[\alpha(n+1)-n]}{2(n+2)+(n+1)(\omega-1)}$	$\frac{\alpha(n+1)(2-\beta)-2n}{2(n+2)-\beta(n+1)}$
F_3-F_2	$\frac{n(\alpha-2)}{n+2}$	$\frac{n[\alpha\kappa-(2\kappa+1)]}{n+1+\kappa(n+2)}$	$\frac{\alpha[2n-(n+1)(\omega-1)]-4n}{2(n+2)+(n+1)(\omega+1)}$	$\frac{\alpha[2n-\beta(n+1)]-4n}{2(n+2)-\beta(n+1)}$

Table 5: Formulation of parameters F_2, F_3 and F_3-F_2 in plane geometry for the following cases: i) plane unbounded; ii) channelized plane flow of parameter κ, the width b of the cross-section is related to its height h by $b \propto y^\kappa$, $\kappa < 1/=/> 1$ corresponds to narrow/triangular/wide cross-sections, with $\kappa \to \infty$ indicating the unbounded case; iii) vertical heterogeneity with permeability varying along y as $k \propto y^{\omega-1}$, $\omega = 1$ corresponds to the homogeneous case; iv) horizontal heterogeneity with permeability varying along x as $k \propto x^\beta$, $\beta = 0$ corresponds to the homogeneous case.

laws of variation of properties. For the case covered in the present paper (radial propagation in an horizontally heterogeneous media) F_2,F_3 and F_3-F_2 are reported in Equations (A.2), (A.3), and (22), respectively. Results for other geometries and/or laws of variation were derived in previous papers [19, 20, 15, 43, 16], always with the parameter α equal to the time exponent of the volume of the current. Table 5 covers results for plane geometry: the base unbounded case [19] is compared to the channelized case of parameter κ [43], to vertical heterogeneity of parameter ω [16], and to horizontal heterogeneity of parameter β [16]; see the Table caption for additional details. Table 6 lists results for radial geometry: the base case [20] is compared to vertical heterogeneity of parameter ω [15], and to horizontal heterogeneity of parameter β (the present paper); again see caption for details.

Figure 12 depicts the behaviour of each key parameter for the homogeneous case as a function of geometry, n, and α. For all cases analysed, the radial geometry implies lower values of all key parameters, with the exception of a continuous injection of very shear-thinning fluids in narrow cross sections. For an instantaneous fluid release (α= 0), an increase of the rheological parameter n in radial geometry leads to F_2 values lower than other geometries, due to mass balance considerations. Among the plane cases, F_2 tends to decrease as the shape factor κ increases, tending to the unbounded

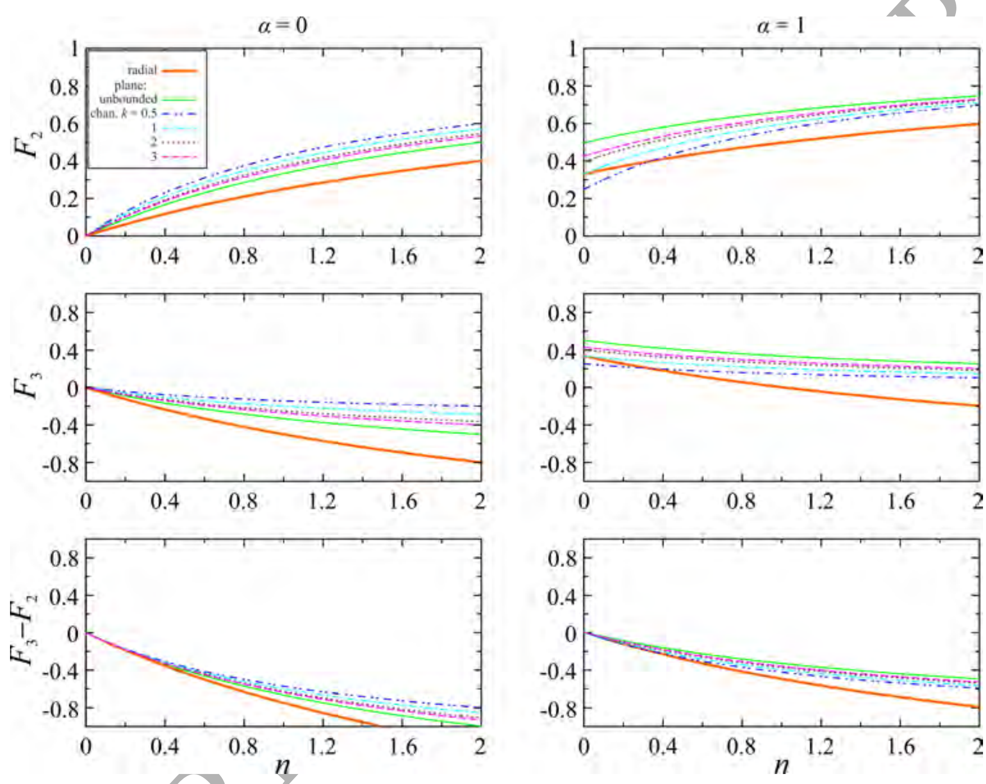

Figure 12: Parameters F_2 (upper row), F_3 (intermediate row) and $F_3 - F_2$ (lower row) as a function of n, for instantaneous ($\alpha = 0$, left column) and continuous injection ($\alpha = 1$, right column), with homogeneous permeability ($\omega = 1$, $\beta = 0$), for radial, plane, and plane channelized geometry of various parameters κ.

	Radial [20]	*Radial, vertical heterogeneity* [15]	*Radial, horizontal heterogeneity* [pp]
F_2	$\dfrac{\alpha+n}{n+3}$	$\dfrac{\alpha[(n+1)(\omega-1)+2]+2n}{2(n+3)+2(n+1)(\omega-1)}$	$\dfrac{2(\alpha+n)}{2(n+3)-\beta(n+1)}$
F_3	$\dfrac{\alpha(n+1)-2n}{n+3}$	$\dfrac{\alpha(n+1)-2n}{2(n+3)+2(n+1)(\omega-1)}$	$\dfrac{\alpha(n+1)(2-\beta)-4n}{2(n+3)-\beta(n+1)}$
F_3-F_2	$\dfrac{n(\alpha-3)}{n+3}$	$\dfrac{\alpha[2n-(n+1)(\omega-1)]-6n}{2(n+3)+2(n+1)(\omega-1)}$	$\dfrac{\alpha[2n-\beta(n+1)]-6n}{2(n+3)-\beta(n+1)}$

Table 6: Formulation of parameters F_2, F_3 and $F_3 - F_2$ in radial geometry for the following cases: i) pure radial; ii) vertical heterogeneity with permeability varying along y as $k \propto y^{\omega-1}$, $\omega = 1$ corresponds to the homogeneous case; iii) horizontal heterogeneity with permeability varying along r as $k \propto r^{\beta}$, $\beta = 0$ corresponds to the homogeneous case. *pp* indicates the present paper.

case ($\kappa \to \infty$), as the volume of the current remains constant and the front of fluid is forced to move further for lower κ. In constant-flux regime (α= 1), radial geometry and $n > 0.5$, F_2 behaves as in the constant-volume regime, while for plane geometries it shows an opposite behaviour, i.e. F_2 increases with higher values of κ. In constant-volume regime (α= 0), the parameter F_3 is negative for all the analysed geometries. In general, this exponent tends to decrease when moving to plane unbounded geometry. In constant flux regime, F_3 is negative only for radial geometry and dilatant fluids ($n > 1$), whilst in plane geometries F_3 tends to increase with the shape factor κ, as does F_2.

For all geometries, the parameter $F_3 - F_2$ is always negative for $\alpha \leq 1$, because of the higher limit of validity for shear thinning fluids. The parameter reaches lower values in constant-volume regime (α= 0), and is larger for plane than for radial geometry. The influence of κ on results is more limited as κ increases. Figure 13 illustrates the trend of parameters F_2,F_3 and $F_3 - F_2$, considering vertical permeability variations in plane and radial geometry. The homogeneous case with ω= 1 [15, 16], is depicted in Figure 12. In both plane and radial geometry, for an instantaneous fluid release (α= 0) and $\omega <$ 1, F_2 is higher than the homogeneous case depicted in Figure 12, whilst it is lower if $\omega > 1$. This trend changes for a constant-flux regime (α= 1). For $\omega < 1$, and plane geometry, F_2 is lower than the homogeneous case, and it becomes higher if $\omega > 1$. In the radial case, for $\omega < 1$, F_2 is lower than

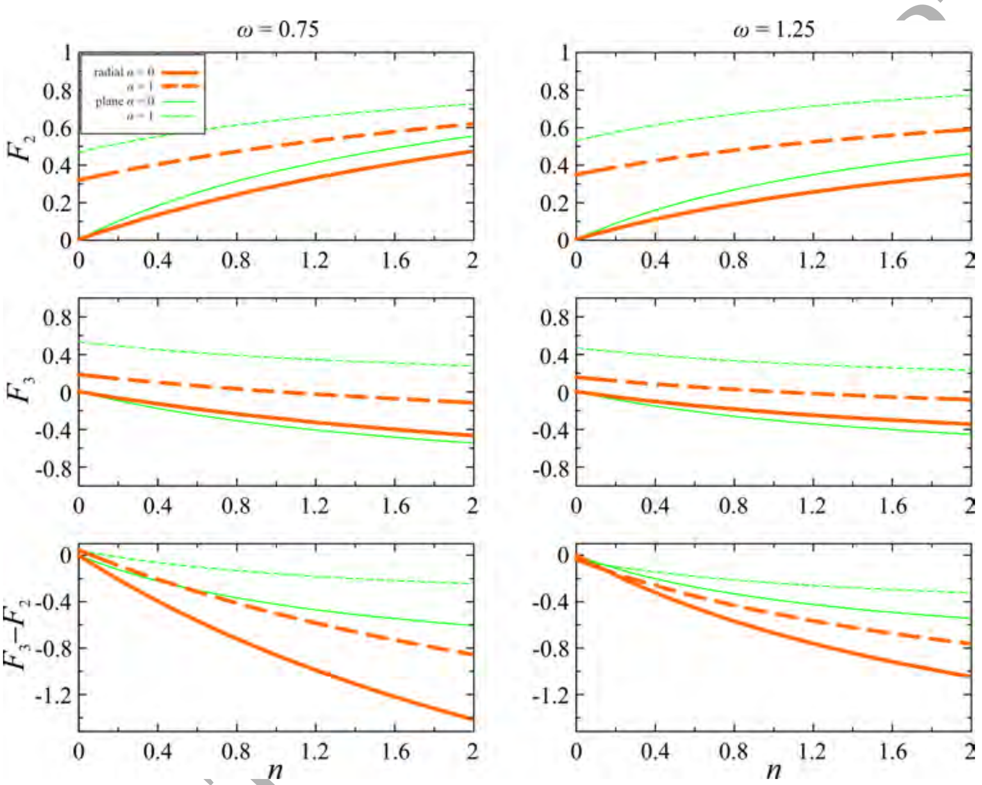

Figure 13: Permeability varying in the vertical direction. Parameters F_2 (upper row), F_3 (intermediate row) and $F_3 - F_2$ (lower row) as a function of n, for permeability decreasing ($\omega = 0.75$, left column) and increasing along the vertical ($\omega = 1.25$, right column), radial/plane geometry (orange/green lines) and instantaneous ($\alpha = 0$, solid line)/continuous ($\alpha = 1$, dashed line) injection.

the homogeneous case, but only for a shear thinning fluid ($n < 1$), while it becomes higher for a dilatant fluid ($n > 1$). On the contrary, if $\omega > 1$, F_2 shows an opposite behaviour.

Concerning the parameter F_3, in constant-volume regime ($\alpha <= 0$) and both geometries, this parameter is lower than the homogeneous case for $\omega < 1$, while it becomes higher if $\omega > 1$. For continuous injection ($\alpha = 1$), in plane unbounded geometry, F_3 is higher than the homogeneous case if $\omega < 1$, and it reverses its behaviour with $\omega > 1$. In radial case, for $\omega < 1$, F_3 is higher than homogeneous case, only for a shear thinning fluid ($n < 1$), while it becomes lower for a dilatant fluid ($n > 1$). On the contrary, if $\omega > 1$, F_3 has an opposite trend.

For an instantaneous release ($\alpha = 0$), in both geometries, $F_3 - F_2$ is lower than the homogeneous case for $\omega < 1$, while it reverses its behaviour if $\omega > 1$. For continuous injection ($\alpha = 1$), in plane unbounded geometry, $F_3 - F_2$ is higher than the homogeneous case if $\omega < 1$, reversing for $\omega > 1$; in radial geometry, instead, the behaviour is similar to F_3. For both geometries, independently on vertical permeability variations, the deviation between homogeneous (Figure 12) and heterogeneous values (Figure 13) tends to increase if n increases for $\alpha = 0$, and it decreases for constant injections only in plane geometry. Figure 14 depicts the behaviour of parameters F_2,F_3 and $F_3 - F_2$, considering horizontal permeability variations in plane and radial geometry; the homogeneous case ($\beta = 0$) is depicted in Figure 12 [16]. In both geometries and regimes, i.e. constant-volume and constant-flux, for $\beta < 0$, F_2 is lower than homogeneous case, while its behaviour is reversed if $\beta > 0$. For $\beta < 0$, the parameter F_3 is higher than the homogeneous case for all geometries and regimes, whilst it becomes lower if $\beta > 0$. Finally, $F_3 - F_2$ follows the same trend of F_3. For both releases, geometries, and horizontal permeability variations, the deviation between homogeneous and heterogeneous case tends to increase for higher n values.

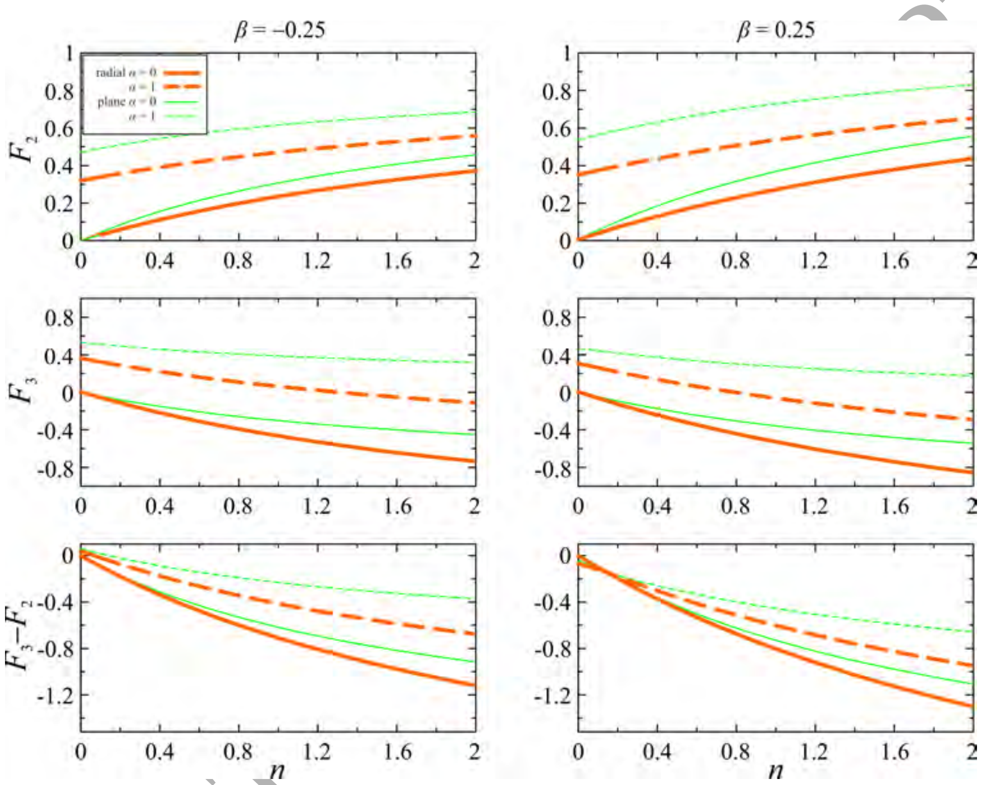

Figure 14: Permeability varying in the horizontal direction. Parameters F_2 (upper row), F_3 (intermediate row) and $F_3 - F_2$ (lower row) as a function of n, for permeability decreasing ($\beta = -0.25$, left column) and increasing along the horizontal ($\beta = 0.25$, right column), radial/plane geometry (orange/green lines) and instantaneous ($\alpha = 0$, solid line)/continuous ($\alpha = 1$, dashed line) injection.

7. Conclusions

We have presented a novel model describing the propagation of axisymmetric power-law GCs in porous media with an horizontal permeability variation. The problem is amenable to a self-similar solution of the first kind yielding the position of the front end and the thickness of the current as functions of dimensionless parameters describing the volume of the GC (α), the fluid rheological behaviour (n), and the power-law permeability variation along the horizontal coordinate (β); depending on the value of β, the permeability increases or decreases with the distance from the origin; in the latter case, this conceptual simplification captures the essential behaviour of the radial variation of permeability around a well, with the additional convenience of an easy-to-implement self-similar solution, which can be used as a benchmark for numerical modelling. The special case of constant volume currents has a closed-form solution. The behaviour of key time exponents governing the rate of propagation, thickness and aspect ratio of the current was discussed in detail, yielding a number of threshold value of model parameters α and β which discriminate between opposite trends in the behaviour of the current over time and govern the sensitivity to model parameters themselves. In turn, these parameters allow to discriminate the conditions for the validity of our solution at large times.

A specific laboratory set-up was devised to directly reproduce horizontal permeability variations, overcoming the difficulties inherent in the horizontal juxtaposition of layers of glass beads of different diameter. Theoretical results were confirmed by our experiments, with a fairly good agreement except for the early-time regime. It is confirmed that also in presence of a deterministic spatial variation of permeability, disturbances or anomalies near the injection line and near the front of the current, do not affect the current evolution in the intermediate asymptotic regime. Also the discretization of the porous medium to mimic a continuous variation of permeability and capillary effects do not significantly affect the behaviour of the GCs, at least for constant influx rate condition ($\alpha = 1$). More important disturbances are expected for constant volume experiments ($\alpha = 0$) and, in general, for waning GCs.

In real applications, model parameters are obtained as follows: i) rheological fluid parameters n and m need to be determined experimentally, bearing in mind that the power-law model is an approximation of the real fluid behaviour; ii) the strength of the injection α depends on its type, which is usually known, and is equal to 0 or 1 for instantaneous or continuous injection; iii) the parameter β reflecting the intensity of the permeability variation needs to be determined experimentally on the basis of available measurements at different locations. Note that two measurements k_1 and k_2 at two locations r_1 and r_2 allow the determination of β by means of Eq. (6).

The theory and experiments herein presented complete a first picture on porous gravity currents of power-law fluid flowing in plane and axisymmetric geometry. The reference solutions are derived by Di Federico *et al.* [19] for plane and by Di Federico *et al.* [20] for radial flow. The influence of channel shape on plane flow is covered in Longo *et al.* [43]. Heterogeneous, deterministic variations of properties are examined by Ciriello *et al.* [16] considering vertical and horizontal grading in 2-D flows, and by Di Federico *et al.* [15] considering vertical grading in radial flow; horizontal grading is covered in the present paper. An overview of the key time exponents for these cases revealed the combination of geometries and model parameters yielding the fastest/lowest currents, and those having the fastest decrease of thickness and aspect ratio over time.

Our study has several connections to geological flows and industrial flows, including flows during fracking procedures, shale gas recovery, drilling wells, and may be relevant for CO_2 sequestration, as solvents which proved effective in CO_2 capture exhibit shear-rate dependent viscosities [44]. In all these applications, fluids exhibiting non–Newtonian effects (often approximated by power-law fluids) are used, almost always in heterogeneous porous media. At the pore-scale, it is worth noting that the effect of heterogeneity prevails over the non linearity due to rheology in shaping the flow pattern [45], with a relatively minor influence of the specific rheological equation [46]; it remains an open question whether this is true at Darcy's scale.

In sum, several avenues of investigation remain open in the area of non–Newtonian GCs, e.g.

- inclusion of fluid drainage/injection at the bottom of the current, either distributed or concentrated in single/multiple fissure(s);
- inclusion of stratification effects in the advancing current;
- consideration of more complex permeability variations, including cut-offs and discontinuities in the medium properties (e.g. inclusions);
- adoption of more realistic rheological models to describe complex fluids, such as Carreau or truncated power-law;

- stochastic modelling of heterogeneity.

We are investigating these fascinating topics and hope to report on them in the near future.

Acknowledgements

We thank Luca Chiapponi for assistance with the laboratory experiments.

Appendix A. Self-similar solution

Inspection of Eq. (10) yields the following time scalings for the length R and thickness H of the current

$$R \sim T^{F_2}, H \sim T^{F_3} \tag{A.1}$$

where

$$F_2 = \frac{2(\alpha + n)}{2(n+3) - \beta(n+1)}, \tag{A.2}$$

$$F_3 = \frac{\alpha(n+1)(2-\beta) - 4n}{2(n+3) - \beta(n+1)}. \tag{A.3}$$

This suggests the adoption of the similarity variable

$$\eta = R/T^{F_2}, \tag{A.4}$$

which in turn leads to the expression of the position of the front and of the thickness respectively as

$$R_N(T) = \eta_N T^{F_2}, \tag{A.5}$$

$$H(R,T) = T^{F_3} f(\eta), \tag{A.6}$$

where η_N is the η value at the front $R = R_N(T)$. The function $f(\eta)$ may be recast as $f(\eta) = \eta_N^{F_5}\psi(\zeta)$ via the introduction of the normalized similarity variable $\zeta = \eta/\eta_N$, where

$$F_5 = \frac{(n+1)(2-\beta)}{2}, \tag{A.7}$$

and $\psi(\zeta)$ is the thickness profile. Substituting $f(\eta)$ in (A.6) gives

$$H(R,T) = \eta_N^{F_5} T^{F_3} \psi(\zeta), \tag{A.8}$$

and adoption of the latter expression for the thickness transforms: i) Eq. (10) into the ODE (13); ii) the condition (12) into (15); iii) the boundary condition (5) into (14). These three equations are reported in the main body of the manuscript.

References

[1] M. Ungarish, An Introduction to Gravity Currents and Intrusions, CRC Press, 2009.

[2] H. E. Huppert, J. A. Neufeld, C. Strandkvist, The competition between gravity and flow focusing in two-layered porous media, J. Fluid Mech. 720 (2013) 5–14. doi:10.1017/jfm.2012.623.

[3] C. K. Sahu, M. R. Flynn, The effect of sudden permeability changes in porous media filling box flows, Transport in Porous Media 119 (1) (2017) 95–118. doi:10.1007/s11242-017-0875-3.

[4] T. D. Ngo, E. Mouche, P. Audigane, Buoyant flow of CO_2 through and around a semi-permeable layer of finite extent, Journal of Fluid Mechanics 809 (2016) 553584. doi:10.1017/jfm.2016.684.

[5] A. Islam, T. Meckel, A. Sun, P. Krishnamurthy, Numerical experiments of density driven CO_2 saturated brine migration in heterogeneous two-dimensional geologic fabric materials, International Communications in Heat and Mass Transfer 71 (2016) 148 – 156. doi:10.1016/j.icheatmasstransfer.2015.12.019.

[6] Y. E. Yu, Z. Zheng, H. A. Stone, Flow of a gravity current in a porous medium accounting for drainage from a permeable substrate and an edge, Phys. Rev. Fluids 2 (2017) 074101. doi:10.1103/PhysRevFluids.2.074101.

[7] E. J. Huber, A. D. Stroock, D. L. Koch, Analysis of a time dependent injection strategy to accelerate the residual trapping of sequestered CO_2 in the geologic subsurface, International Journal of Greenhouse Gas Control 44 (2016) 185 – 198. doi:10.1016/j.ijggc.2015.11.024.

[8] T. V. Ball, H. E. Huppert, J. R. Lister, J. A. Neufeld, The relaxation time for viscous and porous gravity currents following a change in flux, Journal of Fluid Mechanics 821 (2017) 330342. doi:10.1017/jfm.2017.243.

[9] S. S. Pegler, H. E. Huppert, J. A. Neufeld, Stratified gravity currents in porous media, Journal of Fluid Mechanics 791 (2016) 329–357. doi:10.1017/jfm.2015.733.

[10] B. Guo, Z. Zheng, K. W. Bandilla, M. A. Celia, H. A. Stone, Flow regime analysis for geologic CO_2 sequestration and other subsurface fluid injections, International Journal of Greenhouse Gas Control 53 (2016) 284 – 291. doi:10.1016/j.ijggc.2016.08.007.

[11] H. Unwin, G. Wells, A. Woods, CO_2 dissolution in a background hydrological flow, Journal of Fluid Mechanics 789 (2016) 768–784. doi:10.1017/jfm.2015.752.

[12] M. Elenius, D. Voskov, H. Tchelepi, Interactions between gravity currents and convective dissolution, Advances in Water Resources 83 (2015) 77 – 88. doi:10.1016/j.advwatres.2015.05.006.

[13] T. I. Bjornara, J. M. Nordbotten, J. Park, Vertically integrated models for coupled two-phase flow and geomechanics in porous media, Water Resources Research 52 (2) (2016) 1398–1417. doi:10.1002/2015WR017290.

[14] V. Di Federico, S. Longo, S. E. King, L. Chiapponi, D. Petrolo, V. Ciriello, Gravity-driven flow of Herschel-Bulkley fluid in a fracture and in a 2D porous medium, Journal of Fluid Mechanics 821 (2017) 59–84. doi:10.1017/jfm.2017.234.

[15] V. Di Federico, S. Longo., L. Chiapponi, R. Archetti, V. Ciriello, Radial gravity currents in vertically graded porous media: Theory and experiments for Newtonian and power-law fluids, Advances in Water Resources 70 (2014) 65 – 76. doi:10.1016/j.advwatres.2014.04.015.

[16] V. Ciriello, S. Longo, L. Chiapponi, V. Di Federico, Porous gravity currents: A survey to determine the joint influence of fluid rheology and variations of medium properties, Advances in Water Resources 92 (2016) 105 – 115. doi:10.1016/j.advwatres.2016.03.021.

[17] H. E. Huppert, A. W. Woods, Gravity-driven flows in porous layers, J. Fluid Mech. 292 (1995) 55–69. doi:10.1017/S0022112095001431.

[18] S. Lyle, H. Huppert, M. Hallworth, M. Bickle, A. Chadwick, Axisymmetric gravity currents in a porous medium, J. Fluid Mech. 543 (2005) 293–302. doi:10.1017/S0022112005006713.

[19] V. Di Federico, R. Archetti, S. Longo, Similarity solutions for spreading of a two-dimensional non-Newtonian gravity current, J. Non-Newtonian Fluid Mech. 177–178 (2012a) 46–53. doi:10.1016/j.jnnfm.2012.04.003.

[20] V. Di Federico, R. Archetti, S. Longo, Spreading of axisymmetric non-Newtonian power-law gravity currents in porous media, J. Non-Newtonian Fluid Mech. 189–190 (2012b) 31–39. doi:10.1016/j.jnnfm.2012.10.002.

[21] Z. Zheng, B. Soh, H. E. Huppert, H. A. Stone, Fluid drainage from the edge of a porous reservoir, J. Fluid Mech. 718 (2013) 558–568. doi:10.1017/jfm.2012.630.

[22] Z. Zheng, I. C. Christov, H. A. Stone, Influence of heterogeneity on second-kind self-similar solutions for viscous gravity currents, J. Fluid Mech. 747 (2014) 218–246. doi:10.1017/jfm.2014.148.

[23] L. Chiapponi, Water retention curves of multicomponent mixtures of spherical particles, Powder Technology 320 (2017) 646–655. doi:10.1016/j.powtec.2017.07.083.

[24] R. H. Cristopher, S. Middleman, Power-law flow through a packed tube, Ind. Eng. Chem. Fundam. 4 (1965) 422–427. doi:10.1021/i160016a011.

[25] R. B. Bird, W. E. Stewart, E. N. Lightfoot, Transport phenomena, John Wiley & Sons, 1960.

[26] A. V. Shenoy, Non-Newtonian fluid heat transfer in porous media, Adv. Heat Trans. 24 (1995) 102–190. doi:10.1016/S0065-2717(08)70233-8.

[27] H. Pascal, Nonsteady flow of non-Newtonian fluids through a porous medium, Int. J. Eng. Sci. 21 (1983) 199–210. doi:10.1016/0020-7225(83)90021-6.

[28] M. Balhoff, K. Thompson, A macroscopic model for shear-thinning flow in packed beds based on network modeling, Chem. Eng. Sci. 61 (2006) 698719.

[29] M. Vakilha, M. Manzari, Modelling of power-law fluid flow through porous media using smoothed particle hydrodynamics, Transport in Porous Media 74 (2008) 331346. doi:10.1017/S0022112006009578.

[30] N. Yilmaz, A. Bakhtiyarov, R. Ibragimov, Experimental investigation of Newtonian and non-Newtonian fluid flows in porous media, Mech. Res. Comm. 36(5) (2009) 638–641.

[31] V. Ciriello, S. Longo, V. Di Federico, On shear thinning fluid flow induced by continuous mass injection inporous media with variable conductivity, Mech Res Comm 5 (2013) 101–107. doi:10.1016/j.mechrescom.2013.07.006.

[32] G. D. Marsily, Hydrogéologie quantitative, Masson, 1980.

[33] X.-W. Jiang, X.-S. Wang, L. Wan, Semi-empirical equations for the systematic decrease in permeability with depth in porous and fractured media, Hydrogeol. J. 18(4) (2010) 839–850. doi:10.1007/s10040-010-0575-3.

[34] H. C. Slider, Worldwide practical petroleum reservoir engineering methods, PennWell Books, 1983.

[35] A. Altunkaynak, Z. Sen, Steady state flow with hydraulic conductivity change around large diameter wells, Hydrological Processes 25 (11) (2011) 1778–1783. doi:10.1002/hyp.7935.

[36] B. Li, Y. Su, W. Wang, Temporal scale-based production analysis of fractured horizontal wells with stimulated reservoir volume, Journal of Natural Gas Science and Engineering 48 (SI) (2017) 46–64. doi:10.1016/j.jngse.2017.03.006.

[37] D. Vella, H. E. Huppert, Gravity currents in a porous medium at an inclined plane, J. Fluid Mech. 555 (2006) 353–362. doi:10.1017/S0022112006009578.

[38] R. E. Pattle, Diffusion from an instantaneous point source with a concentration-dependent coefficient, Q. J. Mechanics Appl. Math. 4 (1959) 407–409. doi:10.1093/qjmam/12.4.407.

[39] S. Longo, V. Di Federico, L. Chiapponi, R. Archetti, Experimental verification of power-law non-Newtonian axisymmetric porous gravity currents, J. Fluid Mech. 731, R2 (2013b) 1–12. doi:10.1017/jfm.2013.389.

[40] J. G. Savins, Non-Newtonian flow through porous media, Ind. and Eng. Chem. 61 (1969) 18–47.

[41] J. Amundarain, L. Castro, M. Rojas, S. Siquier, N. Ramírez, A. Müller, A. Sáez, Solutions of xanthan gum/guar gum mixtures: shear rheology, porous media flow, and solids transport in annular flow, Rheologica Acta 48 (5) (2009) 491–498. doi:10.1007/s00397-008-0337-5.

[42] L. Zhong, M. Oostrom, M. J. Truex, V. R. Vermeul, J. E. Szecsody, Rheological behavior of xanthan gum solution related to shear thinning fluid delivery for subsurface remediation, Journal of Hazardous Materials 244 (2013) 160–170. doi:10.1016/j.jhazmat.2012.11.028.

[43] S. Longo, V. Ciriello, L. Chiapponi, V. D. Federico, Combined effect of rheology and confining boundaries on spreading of porous gravity currents, Advances in Water Resources 79 (2015) 140–152. doi:10.1016/j.advwatres.2015.02.016.

[44] L. L. Sze, S. Pandey, S. Ravula, S. Pandey, H. Zhao, G. A. Baker, S. N. Baker, Ternary deep eutectic solvents tasked for carbon dioxide capture, ACS Sustainable Chemistry & Engineering 2 (9) (2014) 2117–2123. doi:10.1021/sc5001594.

[45] F. Zami-Pierre, R. de Loubens, M. Quintard, Y. Davit, Transition in the flow of power-law fluids through isotropic porous media, Phys. Rev. Lett. 117 (2016) 074502/1–074502/5.

[46] T. Chevalier, S. Rodts, X. Chateau, C. Chevalier, P. Coussot, Breaking of non-newtonian character in flows through a porous medium, Phys. Rev. E: Stat., Nonlinear, Soft Matter Phys. 89 (2014) 023002.